

## A BROADBAND METAL-MESH HALF-WAVE PLATE FOR MILLIMETRE WAVE LINEAR POLARISATION ROTATION

G. Pisano<sup>\*</sup>, M. W. Ng, V. C. Haynes, and B. Maffei

JBCA, School of Physics and Astronomy, The University of Manchester, United Kingdom

**Abstract**—We present a polarisation rotator based on a dielectrically embedded metal Mesh Half Wave Plate (MHWP) working in the W-band frequency range (75–110 GHz). The device was realised using metallic grids with sub-wavelength anisotropic geometries able to mimic the behaviour of natural birefringent materials. The device was designed using a combination of transmission line codes and finite-element analysis able to achieve phase accuracy down to a fraction of degree. Very accurate intensity and phase measurements were carried out using coherent radiation from a Vector Network Analyser (VNA). The presented device performs better and it is much thinner than previous devices having reduced the number of grids by a factor two and minimised their inductive losses. The new mesh HWP has excellent performances in terms of differential phase-shift flatness and cross-polarisation respectively  $180.4 \pm 2.9^\circ$  and  $-28$  dB across a 25% bandwidth.

### 1. INTRODUCTION

In communication systems polarisation rotators are devices used to rotate the orientation of linearly polarised signals from initial to final specific directions. For example the polarisation direction can be changed from horizontal to vertical and viceversa without rotating any part of the antenna system. These devices can be realised cascading different wire-grid polariser rotated at different angles from each other [1–3]. However, the orientation of the incoming and outgoing polarisation are fixed and related to the device orientation. More flexible devices, based on meander-lines geometries have been realised to obtain arbitrary rotation at microwave frequencies [4].

---

*Received 14 May 2012, Accepted 26 June 2012, Scheduled 6 July 2012*

\* Corresponding author: Giampaolo Pisano (giampaolo.pisano@manchester.ac.uk).

In the field of millimetre-wave astronomy it is often required to continuously rotate the weak incoming linearly polarised signals in order to modulate and extract them from huge unpolarised backgrounds. This is normally achieved by means of rotating Half-Wave Plates (HWPs) that are devices equivalent to arbitrary rotation polarisation rotators. More specifically, in the field of experimental cosmology, the detection of the polarisation of the Cosmic Microwave Background radiation (CMB) requires extremely sensitive broadband instruments with very low-loss and low cross-polarisation HWPs in front of these instruments. In the past these devices were realised using combinations of birefringent plates following the well-known Pancharatnam recipes [5–8]. However, nowadays CMB experiments aiming to the detection of the very faint polarisation B-modes require very large arrays and modulating devices with diameters that cannot be achieved using commercially available birefringent materials. Moreover, the final application in this field will be a satellite mission where these HWPs will be required to be robust, able to work in cryogenic environments and obviously to be space qualified.

The first device aimed to replace the birefringent waveplates was successfully developed using metal mesh grids manufactured using photolithography [9]. Unfortunately, the diameter of these air-gap devices had to be limited to a few centimetres due to the delicate thin substrates (4  $\mu\text{m}$  thick mylar) where the copper grids were deposited. In order to design more robust devices, the well-known technique used to build dielectrically embedded mesh filters [10] has been adopted recently to realise a dielectrically embedded mesh HWP design [11]. However, the reported device showed high losses and phase errors of the order of  $30^\circ$  that make them not suitable for CMB polarimetry applications.

In this work we have:

- adopted the dielectrically embedded technique that allowed us to manufacture a 20 cm diameter mesh HWP;
- used another type of grid design that allowed a reduction of the total number of grids by a factor two, giving a much thinner device with lower losses and with grids that are easier to align;
- developed a transmission line code used in conjunction with finite element analysis that allowed us to achieve phase accuracy on the produced device at the degree level;
- characterised the mesh HWP at millimetre wavelengths using of a Vector Network Analyser that allowed to measure directly the phase-shifts instead of being induced from other measurements, as it was done in the past.

Using this technology we have successfully developed a broadband polariser designed to convert linear to circular polarisation and viceversa at millimetre wavelengths [12,13]. The new dielectrically embedded mesh-HWP presented here is mechanically very robust, it is in excellent agreement with the model predictions and shows unprecedented performance in terms of differential phase-shift and cross-polarisation at millimetre wavelengths.

## 2. MESH HWP DESIGN

The first HWP based on the mesh filters technology [12] was designed adopting the grid geometries suggested by Shatrow [14] used in the past to build polarisers for antenna communications. The HWP consisted of two different stacks of six grids each: one with capacitive and the other with inductive elements, providing opposite phase-shifts. Ideally each stack interacts only with one polarisation, creating a specific phase-shift, and looks almost transparent to the orthogonal one. The stacks were rotated by  $90^\circ$  in order to act independently on the two polarisations providing an almost constant differential phase-shift close to  $180^\circ$  across a 30% bandwidth centered at 150 GHz.

In order to manufacture a more robust device it is possible to embed the metal grids inside a dielectric material. This technique, extensively used in the past to develop space qualified mesh filters [10], has been used recently to realise a dielectrically embedded mesh HWP [11]. This design relied again on the Shatrow-type geometry, still requiring a total of 12 grids to achieve a phase-shift of  $180^\circ$ . However, the non-ideal performance of this device in terms of losses and phase errors was probably related to the copper thickness deposition and on the practical difficulties arising in the alignment of 12 different grids during its manufacture.

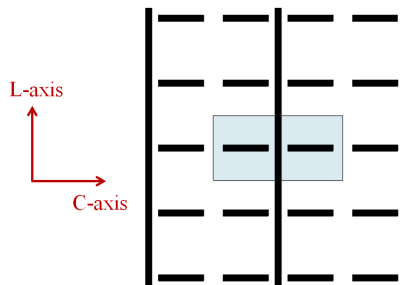


**Figure 1.** Metal mesh Lerner-type geometry with highlighted periodic single-cell.

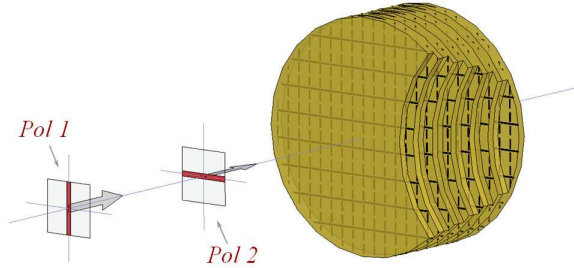


**Figure 2.** Sketch of the dielectrically embedded six grids Mesh-HWP internal structure.

In our design we did solve the above problems by evaporating much more copper in each substrate ( $2\ \mu\text{m}$ ) and in adopting the grid geometry suggested by Lerner [15]. This geometry allows having both the capacitive and inductive elements interacting with the two orthogonal polarisations, on the same grid (Fig. 1). A sketch of the six-grids dielectrically embedded mesh HWP presented in this work is shown in Fig. 2. The vertical polarisation *Pol-1* going through the plate will interact with the capacitive grids (dashed lines) whereas the horizontal polarisation *Pol-2* will experience the inductive behaviour of the parallel lines. The overall effect of the six grids is to create a differential phase-shift of  $180^\circ$  between the two polarisations over a broad bandwidth, as required by an achromatic HWP.

There are at least three advantages in adopting the Lerner-type grid geometry for the design of a mesh-HWP:

- i) the total number of grids is reduced by a factor two with associated reduction in losses;
- ii) the orthogonality between capacitive and inductive elements in each grid is guaranteed by the extremely high accuracy of the photolithographic processes;
- iii) the alignment between the grids, now reduced down to six, is much easier to be achieved.

### 3. MESH HWP MODELLING

Mesh filters can be modelled with good approximation using the transmission line theory, identifying the single grids with electric lumped elements [16,17]: there are analytical formulae to describe a variety of grid geometries in the literature. However, in designing retarding surfaces, such as mesh HWPs, the phase information becomes

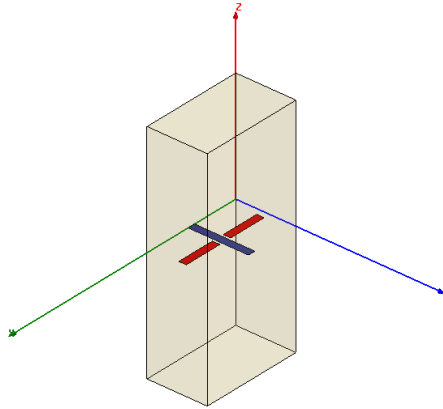


**Figure 3.** Lerner-type geometry single-cell HFSS model.

a critical parameter and the available lumped element formulae are not accurate enough to guarantee the design of high performance devices.

In order to solve this problem, it is possible to use finite-element analysis in conjunction with transmission line codes. We did use the commercial software Ansys HFSS [18] to accurately model a single cell of the Lerner grid geometry under study (see Fig. 3). From the computed scattering matrix coefficients it was possible to de-embed the equivalent lumped element admittances of the grids and to obtain frequency dependent admittances far more accurate than those determined analytically. Moreover, these results also included the losses coming from the finite conductivity of the copper grids and from the non-ideal dielectric substrates that are normally not taken into account.

The transmission line (TL) code, written with a classic programming language, was fed with the new computed admittances to predict the transmission and the phase behaviour of the mesh HWP along both axes. The code allowed the prediction of the phase behaviour of the final device with an accuracy of the order of a few degrees. The designing phase consisted of running an optimisation procedure where the goal was to maximise and equalise the averaged transmission along both axes and obtain a differential phase-shift error below  $1^\circ$  across a 25% bandwidth, centered around 90 GHz. The parameters involved in the optimisation were the dielectric spacing between the six grids and the use of different grid geometries previously de-embedded with HFSS.

Once a design meeting the above requirements was obtained, the new design was entirely checked with finite-element analysis (HFSS)

simulating a single cell of the whole device (including the six grids, the dielectric material and both polarisations). We noticed that it would have not be practically possible to design and optimise the device using these global models on their own without the first TL optimisation. This is due to the long computational times associated with these simulations: although these models are not particularly large, the number of iterations required to achieve phase accuracy below one degree can be very high. The results of these final HFSS simulations were very close to the transmission line code predictions in terms of transmission amplitudes. However, they sometimes differed by a few degrees in the more critical differential phase-shift parameter. Therefore a final fine-tuning optimisation, completely based on HFSS was eventually carried out in order to get the differential phase-shift of the whole device within  $1^\circ$  from the required  $180^\circ$ . This last fine-tuning required only a few iterations. The expected axes transmission, phase-shifts, differential phase-shift and cross-polarisation for both the transmission line and the finite-element analysis models are reported respectively in Figs. 8, 9,10,11 and 12 together with the experimental results that will be discussed in details in Section 6.

#### 4. MESH HWP MANUFACTURE

The production of the mesh HWP was divided in different phases. Initially, it was necessary for the photolithographic processes to produce masks with the required grid geometries. Copper was then evaporated on thin polypropylene (PP) substrates mounted on metallic rings. The copper thickness was of the order of  $2\ \mu\text{m}$ , much more than the required 200 nm skin depth, in order to avoid the additional losses due to breaking of the inductive lines during the thermal bonding. Photoresist coatings were deposited on the copper evaporated PP

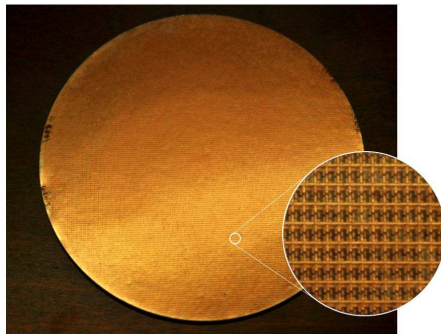


**Figure 4.** Prototype picture with grids details.

substrates and then UV exposed through the masks: the copper was then etched away leaving the desired patterns. Before proceeding further, these single grids were electromagnetically tested in order to select the best ones to be used for the final stack (see Section 5). Accurate grid spacing was achieved stacking tens of thin PP layers with thicknesses starting from  $36\ \mu\text{m}$ . Very accurate alignment of the grids was required to avoid cross-polarisation effects. The whole stack was then clamped and heated up in a vacuum oven. All the layers were bonded together to form the final single block device. A prototype of the W-band mesh-HWP is shown in Fig. 4: the device has a diameter of 20 cm and is 4.5 mm thick.

## 5. EXPERIMENTAL SETUP AND SINGLE GRID TESTS

The mesh HWP tests were performed using a Vector Network Analyser Rohde and Schwarz ZVA40 equipped with two WR10 waveguide converter heads allowing to explore the W-band frequency range: 75–110 GHz. The signals from the VNA heads were launched in free space by means of corrugated horns in order to create almost pure Gaussian beams. The experimental setup is shown in Fig. 5. This type of measurements are based on coherent radiation and allow the acquisition of both the amplitude and the phase of the transmitted electric fields. This allows the possibility to directly measure the phase-shift induced by our device rather than deduce it from cross-polarisation measurements as it was done for previous devices [11] using a Fourier Transform Spectrometer (FTS). In the latter case it is not possible to access directly the phase information, the method being based on intensity measurements.

The drawback in using a coherent source like a VNA is the creation of standing waves arising between the plates and the horns. These effects can be strongly reduced using the test setup sketched in Fig. 5:

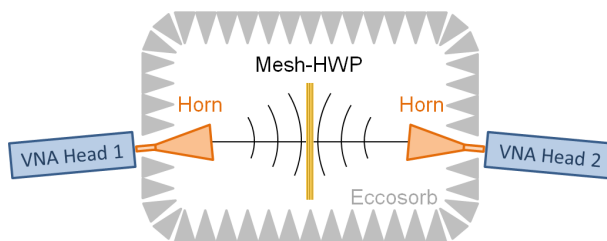


**Figure 5.** Experimental setup for the Mesh-HWP electromagnetic characterisation.

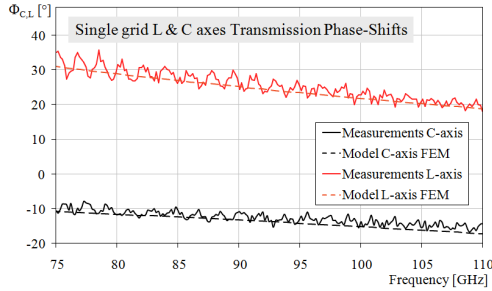


**Figure 6.** Single grid transmission phase measurements along capacitive and inductive axes.

the horn antennas are slightly misaligned to force most of the reflected radiation to go outside the optical path and to be absorbed by the Eccosorb walls [19]. The horns are positioned such that the radiation going through the plate and then detected is still perpendicular to the plate under study. Due to the symmetry of the setup, with the horns polarisation perpendicular to the plane of the figure, the cross-polarisation is in principle null. In practice the system cross-polarisation is of the order of  $-45$  dB, setting the accuracy level of these measurements.

As mentioned earlier, during the device manufacture all the grids were individually tested with the VNA. The best grids were then selected and used for the final device. Examples of transmission phase measurements along the two orthogonal axes of a single grid are reported in Fig. 6. There is very good agreement between the experimental results and the model predictions. Direct phase measurements of this type have never been performed before in the development of mesh HWPs.

## 6. MESH-HWP EXPERIMENTAL CHARACTERISATION

The transmission measurements of the mesh-HWP were performed aligning alternatively the capacitive and the inductive axes of the plate with the incoming electric field direction (see the *Co-Pol C* and *Co-Pol L* measurements setup in Figs. 7(a) and 7(c) respectively). The initial polarisation direction was defined by the rectangular waveguide port of the first VNA head; the polarisation of the second port was aligned with the first one. The scattering matrix parameter  $S_{21}$ , representing the amplitude of the electric field coming from *port* 1 and

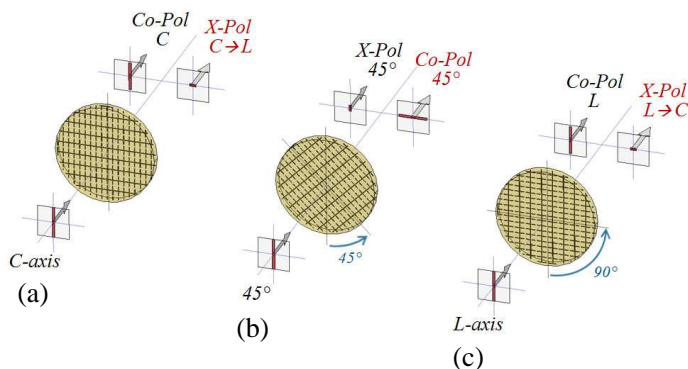


**Figure 7.** Mesh-HWP transmission and cross-polarisation measurements setup.

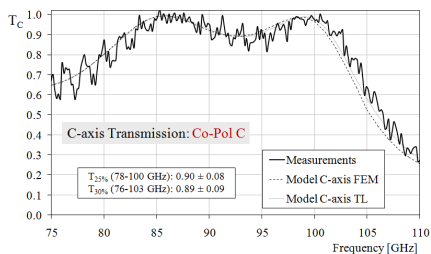


**Figure 8.** Mesh-HWP capacitive axis intensity transmission: Finite Element (FEM) and Transmission Line (TL) simulations against measurements.

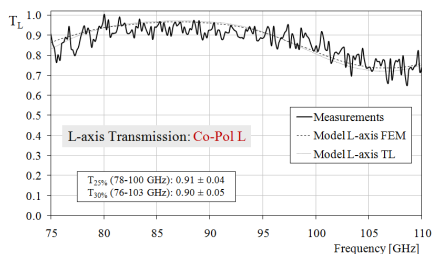


**Figure 9.** Mesh-HWP inductive axis intensity transmission simulations and measurements.

measured on *port 2*, was acquired each time across the whole W-band. Immediately after each axis measurement, another measurement was taken without the device in place in order to acquire the transmission background. The final device transmissions were deduced simply normalising the axes measurements to their backgrounds. Figs. 8 and 9 show the transmission intensity results along the capacitive and inductive axes of the mesh-HWP together with the transmission line and the finite-element analysis model predictions. It is clear that there is a very good agreement between experimental data and simulations. Across the 78–100 GHz frequency range (25% bandwidth) the averaged transmission measurements of the capacitive and inductive axes gave respectively:  $T_C = 0.90$  and  $T_L = 0.91$ .

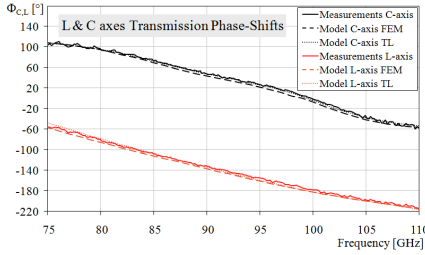


**Figure 10.** Mesh-HWP transmission phase-shift simulations and measurements along the  $C$ - and  $L$ -axis.

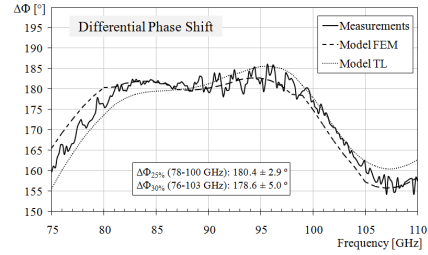


**Figure 11.** Mesh-HWP differential phase-shift measurements and simulations.

The VNA transmission data inherently includes phase information that can be extracted simply calculating the argument of these background-normalised complex data sets. The phase-shifts associated to the capacitive and inductive axes of the mesh-HWP are both reported in Fig. 10. The measured phases show a small systematic constant drift of a few degrees in the positive direction at all frequencies and along both axes. This is probably due to a systematic error in the measurements, arising from the finite thickness of the plate, equally affecting both axes. However, being this systematic phase-shift error almost identical along the two axes, it does not affect the overall performance of the mesh-HWP, as it will be showed in the following paragraphs.

Accurate differential-phase measurements with errors below the degree level are very difficult to perform. The VNA drifts are actually much larger for the phase than for the amplitude. The differential phase-shift between the capacitive and inductive axes could be calculated directly from the difference of the two curves in Fig. 10. However, the relative transmission measurements have to be taken one immediately after the other in order to drastically reduce the VNA phase drifts. Background measurements are not required in this case and the differential phase-shift can be obtained calculating directly the argument of the ratio of the two (not background normalised) axes transmissions. Fig. 11 shows the excellent agreement between the experimental and the simulated differential phase-shift achieved using this technique. Across the frequency range 78–100 GHz the differential phase-shift is  $\Delta\Phi = 180.4 \pm 2.9^\circ$ .

Another important critical parameter to be investigated is the cross-polarisation introduced by the mesh-HWP. There are three cross-polarisation measurements of interest: i) the leakage of a linearly

polarised signal parallel to the  $C$ -axis detected along the  $L$ -axis:  $X$ - $Pol$   $C \rightarrow L$  in Fig. 7(a); ii) the same type of leakage from the  $L$ - to the  $C$ -axis:  $X$ - $Pol$   $L \rightarrow C$  in Fig. 7(c); iii) the residual signal left along the incoming polarisation direction when the HWP is rotated by  $45^\circ$  and the signal is supposed to be rotated by  $90^\circ$ :  $X$ - $Pol$   $45^\circ$  in Fig. 7(b).

The  $X$ - $Pol$   $45^\circ$  measurements were carried out using the same setup used for the transmission tests, this time orienting the waveplate axes at  $45^\circ$  from the incoming electric field direction. This incoming linearly polarised beam can be decomposed into two in-phase components parallel to the waveplate axes. By definition, these components will come out from the plate completely out-of-phase, i.e., with a differential phase-shift of  $180^\circ$ , and so the outgoing polarisation will be orthogonal to the incoming one ( $C$ - $Pol$   $45^\circ$  in Fig. 7(b)). Being the second waveguide port of the experimental setup aligned with the first one, a null cross-polarisation signal would be ideally expected. In the real mesh-HWP, the combination of differential phase-shift not exactly equal to  $180^\circ$  and the axes transmission amplitudes not coincident across the band creates a cross-polar leakage ( $X$ - $Pol$   $45^\circ$  in Fig. 7(b)). Fig. 12 shows the very good agreement between the mesh-HWP cross-polarisation measurements and the model predictions. Across the 78–100 GHz frequency range, the averaged cross-polarisation resulted to be:  $X$ - $Pol$  ( $45^\circ$ ) =  $-28$  dB.

The  $X$ - $Pol$   $L \rightarrow C$  and  $C \rightarrow L$  measurements were carried out rotating the second VNA head by  $90^\circ$  around the optical axis in order to detect the orthogonal leakage component. In principle these signals should be null due to the symmetry of the device. In practice the non-ideal alignment of the grids will create a small cross-

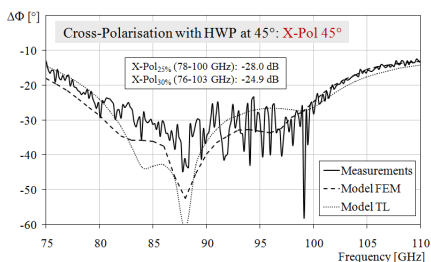


**Figure 12.** Mesh-HWP cross-polarisation measurements corresponding to the test set-up shown in Fig. 7(b).

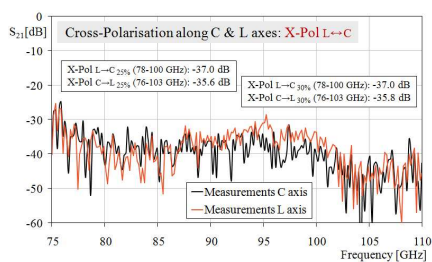


**Figure 13.** Mesh-HWP cross-polarisation measurements along capacitive and inductive axes corresponding to the test set-up shown in Figs. 7(a) and 7(c).

polarisation component. The measurements for both the  $L \rightarrow C$  and  $C \rightarrow L$  configurations are shown in Fig. 13: averaged across the 78–100 GHz frequency range they resulted respectively  $X\text{-Pol}(L \rightarrow C) = -37$  dB and  $X\text{-Pol}(C \rightarrow L) = -35.8$  dB.

## 7. CONCLUSIONS

Accurate and arbitrary polarisation rotation can be achieved by means of Mesh-HWPs based on photolithography. These devices represent a very promising alternative to the more expensive and dimensions-limited birefringent HWPs. The mesh-HWP device presented in this work shows excellent performance in terms of phase error and cross-polarisation that has never been achieved before using this technology. Across a 25% bandwidth (78–100 GHz) the transmissions along the capacitive and inductive axes are respectively  $T_C = 0.90$  and  $T_L = 0.91$ ; the differential phase-shift is  $\Delta\Phi = 180.4 \pm 2.9^\circ$ ; the cross-polarisation along the  $C$ -axis,  $L$ -axis and with the HWP rotated by  $45^\circ$  are respectively  $-37$  dB,  $-35.8$  dB and  $-28$  dB.

The achievement of these results was due to the following improvements in comparison with the previously presented devices: i) the use of the Lerner-type grid geometry that resulted in a thinner device with the number of grids reduced by a factor two, lower losses, easier alignment between grids and inherent photolithographic alignment between capacitive and inductive axes in each grid; ii) extremely accurate modelling based on the combination of finite-element analysis and transmission-line codes that allowed the realisation of devices with phase errors at the degree level; iii) very accurate VNA tests that included direct phase measurements (not induced) and almost instantaneous background normalisation; iv) the use of much thicker copper evaporated layers that drastically reduced the inductive losses reported previously.

Having achieved the control of the transmission phase down to a fraction of degree, this photolithographic technology makes now possible to realise more sophisticated retarding surfaces, where the phase-shift can be designed to vary across their surface. For example, the phase profile generated by a normal dielectric lens could be reproduced by a much thinner and flat ‘mesh-lens’.

## ACKNOWLEDGMENT

We are grateful to the UK Engineering and Physical Sciences Research Council (EPSRC) for the support of this work through the grant EP/H021299/1 at the University of Manchester.

## REFERENCES

1. Torres, R. P. and M. F. Catedra, "Analysis and design of a two-octave polarization rotator for microwave frequency," *IEEE Trans. Microw. Ant. Prop.*, Vol. 41, No. 2, 208–213, 1993.
2. Gimeno, B., J. L. Cruz, E. A. Navarro, and V. Such, "A polarizer rotator system for three-dimensional oblique incidence," *IEEE Trans. Microw. Ant. Prop.*, Vol. 42, No. 7, 912–919, 1994.
3. Lech, R., M. Mazur, and J. Mazur, "Analysis and design of a polarizer rotator system," *IEEE Trans. Microw. Ant. Prop.*, Vol. 56, No. 3, 844–847, 2008.
4. Wu, T., "Meander-line polarizer for arbitrary rotation of linear polarization," *IEEE Micr. Guid. Wav. Lett.*, Vol. 4, No. 6, 199–201, 1994.
5. Pancharatnam, S., "Achromatic combinations of birefringent plates," *Raman Research Inst. Bangalore Memoir*, Vol. 71, 137–144, 1955.
6. Murray, A. G., A. M. Flett, G. Murray, and P. A. R. Ade, "High efficiency half-wave plates for submillimetre polarimetry," *Infr. Phys.*, Vol. 33, 113–125, 1992.
7. Pisano, G., G. Savini, P. A. R. Ade, V. Haynes, and W. K. Gear, "Achromatic half-wave plate for submillimetre instruments in CMB astronomy: Experimental characterisation," *Applied Optics*, Vol. 45, No. 27, 6982–6989, 2006.
8. Savini, G., G. Pisano, and P. A. R. Ade, "Achromatic half-wave plate for submillimetre instruments in CMB astronomy: Modelling and simulation," *Applied Optics*, Vol. 45, No. 35, 8907–8915, 2006.
9. Pisano, G., G. Savini, P. Ade, and V. Haynes, "A metal-mesh achromatic half-wave plate for use at submillimetre wavelengths," *Applied Optics*, Vol. 47, No. 33, 6251–6256, 2008.
10. Ade, P. A. R., G. Pisano, C. E. Tucker, and S. O. Weaver "A review of metal mesh filters," *Proc. SPIE*, Vol. 6275, U2750, 2006.
11. Zhang, J., P. A. R. Ade, P. Mausekopf, G. Savini, L. Moncelsi, and N. Whitehouse, "Polypropylene embedded metal mesh broadband achromatic half-wave plate for millimeter wavelengths," *Applied Optics*, Vol. 50, No. 21, 3750–20757, 2011.
12. Pisano, G., M. W. Ng, V. Haynes, and B. Maffei, "A broadband photolithographic polariser for millimetre wave applications," *PIERS Proceedings*, 1748–1751, Kuala Lumpur, Malaysia, March 27–30, 2012.

13. Maffei, B., G. Pisano, M. W. Ng, and V. Haynes, "Millimetre wave photolithographic polariser beam impact," *PIERS Proceedings*, 1761–1765, Kuala Lumpur, Malaysia, March 27–30, 2012.
14. Shatrow, A. D., A. D. Chuprin, and A. N. Sivov, "Constructing the phase converters consisting of arbitrary number of translucent surfaces," *IEEE Trans. Antennas Propag.*, Vol. 43, No. 1, 1995.
15. Lerner, D. S., "A wave polarization converter for circular polarization," *IEEE Trans. Antennas Propag.*, Vol. 15, 3–7, 1964.
16. Marcuvitz, N., *Waveguide Handbook*, M.I.T. Rad. Lab. Ser., Mc.Graw-Hill, 280–290, 1951.
17. Ulrich, R., "Far-infrared properties of metallic mesh and its complementary structure," *Infrared Physics*, Vol. 7, 37–50, 1967.
18. Ansys High Frequency Structure Simulator: [www.ansys.com](http://www.ansys.com).
19. Emerson & Cuming, Microwave Products, <http://www.eccosorb.com/>.